*Advanced Energy Materials*

ADVANCED ENERGY MATERIALS
www.advenergymat.de

RESEARCH ARTICLE OPEN ACCESS

# Localized Heterogeneous Nucleation for Vapor-Assisted Sequential Deposition of Metal Halide Perovskites

Sung-Eun Kim[1,2] | Seung-Gu Choi[1,2] | Seo-Ryoung Lee[3] | Do-Kyoung Lee[4,5] | Tim Kodalle[5,6] | Byung Soon Kim[7,8] | Jae-Hwan Kim[3] | Keonwoo Park[2,9] | Jaehyeong Lee[7] | Carolin M. Sutter-Fella[5] | Jin-Wook Lee[2,3,10]

[1]Department of Nano Engineering and Department of Nano Science and Technology, SKKU Advanced Institute of Nanotechnology (SAINT), Sungkyunkwan University, Suwon, Republic of Korea | [2]Research Institute of Energy and Resources, Seoul National University, Seoul, Republic of Korea | [3]Department of Energy Systems Engineering, College of Engineering, Seoul National University, Seoul, Republic of Korea | [4]Nevada Extreme Conditions Laboratory University of Nevada, Las Vegas, Nevada, USA | [5]Molecular Foundry Division, Lawrence Berkeley National Laboratory, Berkeley, California, USA | [6]Advanced Light Source Lawrence Berkeley National Laboratory, Berkeley, California, USA | [7]Department of Electrical and Computer Engineering, Sungkyunkwan University, Suwon, Republic of Korea | [8]Sunic System Co., Ltd., Suwon, Republic of Korea | [9]UNIST InnoCORE AI-Space Solar Initiative, Ulsan National Institute of Science and Technology (UNIST), Ulsan, Republic of Korea | [10]School of Transdisciplinary Innovations, Seoul National University, Seoul, Republic of Korea

**Correspondence:** Carolin M. Sutter-Fella (csutterfella@lbl.gov) | Jin-Wook Lee (jinwooklee@snu.ac.kr)

**Received:** 2 January 2026 | **Revised:** 27 February 2026 | **Accepted:** 8 March 2026

**Keywords:** nucleation | perovskite | sequential deposition | solar cell | thermal evaporation

## ABSTRACT

Vapor-assisted hybrid two-step deposition, which combines thermally evaporated inorganic layers with solution-processed organic halides to form halide perovskites, has emerged as a scalable and industry-compatible route for textured tandem photovoltaics. However, this process is often hindered by reaction-limited phase formation, particularly when compact, non-porous, and highly crystalline inorganic layers formed by thermal evaporation restrict subsequent conversion, resulting in incomplete reaction and pronounced depth-dependent heterogeneity. In this study, we introduce a strategy to regulate the inorganic precursor layer by incorporating localized heterogeneous nucleation sites. Sparsely distributed hydrophilic metal oxide species serve as effective nucleation centers during vapor deposition, enabling effective control over film morphology and crystal orientation from the early stages of growth. This tailored inorganic framework facilitates the subsequent incorporation of organic halides, alleviating reaction limitations and suppressing residual unreacted precursors. Consequently, the perovskite films exhibit improved stoichiometric uniformity and enhanced optoelectronic quality, enabling wide-bandgap perovskite solar cells with markedly improved performance and operational stability. This work provides important mechanistic insight into crystal growth engineering of vapor-deposited perovskite thin films.

## 1 | Introduction

Metal halide perovskite solar cells (PSCs) have rapidly advanced to power conversion efficiencies comparable to those of established commercial photovoltaic technologies [1, 2]. In particular, wide-bandgap PSCs employed as top cells in perovskite/silicon tandem architectures have enabled certified efficiencies exceeding 34% [3], accelerating industrial investment in manufacturing technologies that ensure scalability, reproducibility, and process compatibility. In this regard, vacuum-based deposition routes have attracted growing attention as a promising pathway toward large-area and reproducible perovskite fabrication, as

Sung-Eun Kim, Seung-Gu Choi, and Seo-Ryoung Lee contributed equally to this work.

they avoid solvent-related issues inherent to solution processing [4, 5].

Despite these advantages, translating the high performance achieved in solution-processed PSCs to their vacuum-processed counterparts remains challenging. This difficulty arises from fundamental differences in precursor states, processing environments, and crystallization kinetics between vapor deposition and solution-based routes [4, 5]. Consequently, compared with the extensive understanding developed for solution processing, systematic strategies for controlling phase formation and crystallization kinetics during vapor deposition remain relatively underdeveloped.

Among vacuum-compatible approaches, vapor-assisted hybrid two-step deposition, combining a thermally evaporated inorganic layer with the subsequent introduction of an organic halide via solution processing, has emerged as a scalable and commercially viable route, particularly for textured tandem applications [6–9]. In such sequential processes, achieving a complete and well-controlled reaction between the inorganic framework and the organic halide precursor is critical for realizing efficient and stable PSCs. Previous studies on solution-based sequential deposition have demonstrated that reaction kinetics and phase formation are highly sensitive to the morphology and crystallographic orientation of the inorganic layer, motivating extensive efforts to engineer the inorganic framework based on solution processes [10–12]. By contrast, strategies for regulating compact, non-porous inorganic layers formed by thermal evaporation—which present a substantial energetic barrier to organic species diffusion—remain insufficiently explored [13–15].

Here, we present a strategy to regulate the morphology and crystallographic orientation of vapor-deposited inorganic frameworks by deliberately controlling heterogeneous nucleation during film growth. Metal oxide nanoparticles are introduced as localized heterogeneous nucleation sites, enabling controlled modulation of film morphology and crystal orientation from the initial stages of vapor deposition. Topographical and crystallographic analyses reveal pronounced changes in film morphology and structure, while in situ photoluminescence and absorption measurements elucidate the resulting reaction kinetics during perovskite formation. Finally, wide-bandgap PSCs based on the regulated inorganic framework achieve power conversion efficiencies exceeding 21%, together with markedly improved photo- and thermal stability.

## 2 | Result and Discussion

We investigated a representative model system for the hybrid two-step deposition process, in which an inorganic framework was deposited by thermal co-evaporation of $PbI_2$ and CsBr, followed by a second-step reaction with organic halide precursors (FAI/FABr) to form a wide-bandgap perovskite absorber (Figure 1a,b). Consistent with previous reports, X-ray diffraction (XRD) patterns of the as-deposited inorganic templates exhibit a strong preferential orientation along the (001) direction, accompanied by higher-order reflections such as the (002) and (003) planes (Figure 1a) [16]. This pronounced texture originates from the layered crystal structure and dense atomic packing characteristic of thermally evaporated $PbI_2$-based films.

Notably, a diffraction peak corresponding to the inorganic $PbI_2$ precursor persists even after reaction with the organic halide precursors, indicating incomplete conversion. Quantitative analysis reveals that the area ratio between the residual $PbI_2$ (001) peak and the perovskite (100) peak reaches 28.1%, confirming that a substantial fraction of $PbI_2$ remains unreacted. To further elucidate the compositional heterogeneity, time-of-flight secondary ion mass spectrometry (ToF-SIMS) was performed on the resulting perovskite film (Figure 1c). Both 1D depth profiles and 3D ion mapping reveal a pronounced vertical compositional gradient: $FA^+$ ions are enriched near the top surface, whereas $Pb^+$ ions are concentrated toward the bottom interface. This depth-dependent distribution indicates the coexistence of unreacted FAX near the film surface and residual $PbI_2$ at the buried perovskite/substrate interface.

In the sequential deposition process, the conversion of $PbI_2$ into the perovskite phase is initiated by intercalation of $FA^+$ cations into the layered $PbI_2$ framework, followed by reconstruction of the Pb-I lattice into corner-sharing $PbX_6$ octahedra [17]. However, the dense and highly crystalline nature of the evaporated $PbI_2$ template severely limits $FA^+$ diffusivity [15, 18, 19]. As a result, the reaction predominantly occurs near the surface, where $PbI_2$ is readily accessible to the organic halide. Once a perovskite layer forms at the interface, it further impedes downward diffusion of $FA^+$, kinetically trapping unreacted $PbI_2$ near the bottom interface while leaving excess FAX near the top surface (Figure 1d). Such residual precursors introduce defect states and energetic barriers that are detrimental to charge transport, ultimately compromising the performance and operational stability of PSCs [20–22].

During vapor deposition of inorganic layers, vaporized precursors undergo heterogeneous nucleation on the substrate, and the initially crystallized domains subsequently act as a templating layer that governs the growth mode of the entire film [23]. On a flat ITO substrate uniformly modified with the hole-transporting layer, [4-(3,6-dimethyl-9H-carbazol-9-yl)butyl]phosphonic acid (Me-4PACz), vaporized inorganic precursors nucleate uniformly and preferentially adopt a (001) orientation (Figure 2a) [24]. Subsequent adatoms are preferentially adsorbed onto these initial nuclei, resulting in a compact and highly oriented crystalline inorganic layer. To modulate the nucleation behavior and initial growth morphology of the inorganic layer, we drew inspiration from recent inverted p-i-n device architectures in which oxide nanoparticles are introduced to induce selective contact formation [25]. Here, $Al_2O_3$ nanoparticles (NPs) were incorporated to act as localized heterogeneous nucleation sites. Compared with the relatively hydrophobic Me-4PACz/ITO surface with low surface energy, the $Al_2O_3$ NP surface possesses a higher surface energy. We therefore hypothesize that $Al_2O_3$ NPs serve as energetically favorable nucleation centers for vapor-deposited inorganic precursors, enabling deliberate modulation of film morphology and crystallographic orientation (Figure 2a) [26].

To validate this concept, the surface topography of control substrates (bare ITO/Me-4PACz) and substrates modified with $Al_2O_3$ NPs, as well as the corresponding inorganic films grown

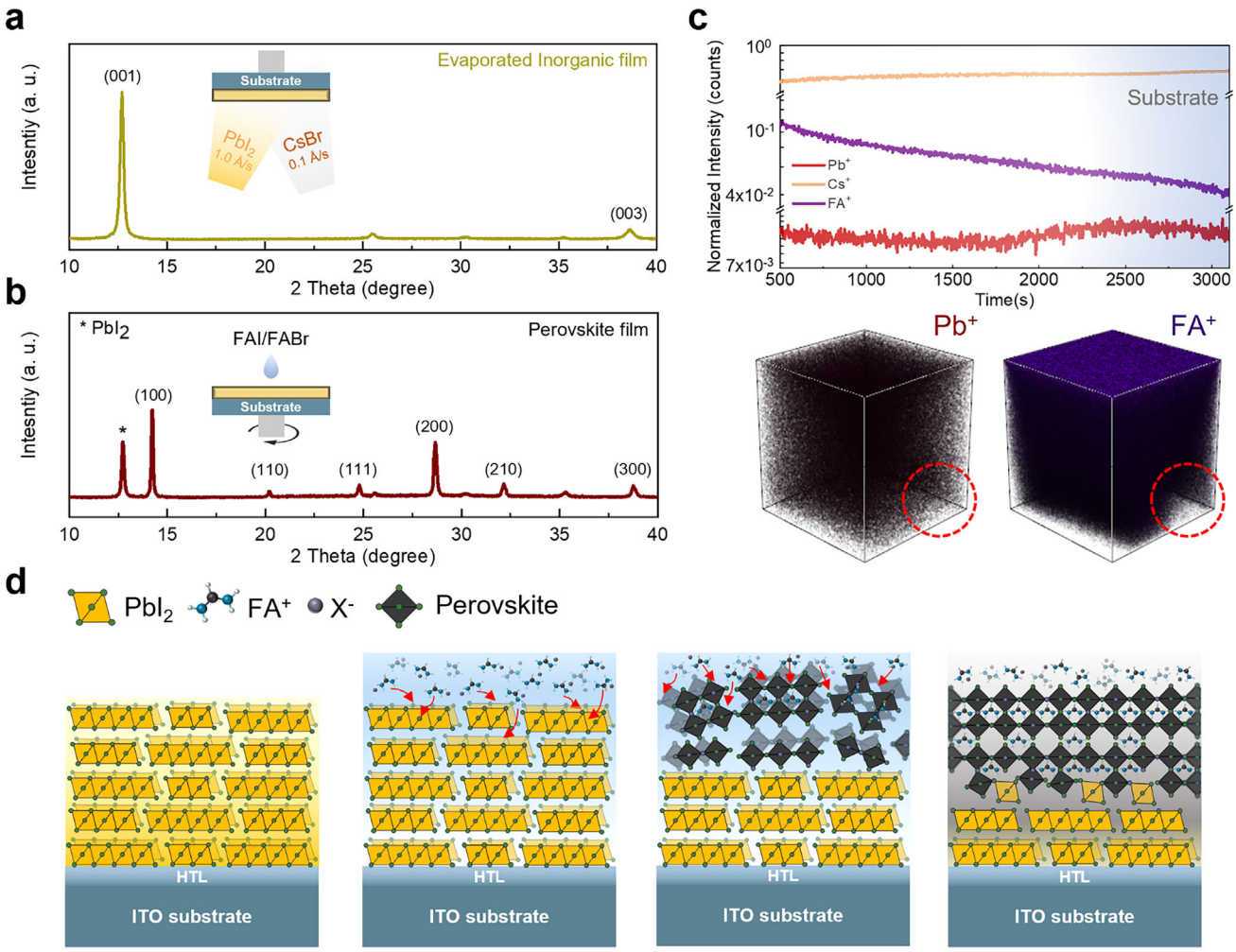


**FIGURE 1** | X-ray diffraction (XRD) patterns of (a) the vacuum-deposited inorganic layer formed by thermal co-evaporation of $PbI_2$ and CsBr and (b) the perovskite film obtained after reaction of the inorganic layer with an FAI/FABr solution. (c) 1D depth profiles and 3D ion mapping acquired by time-of-flight secondary ion mass spectrometry (ToF-SIMS) for the resulting perovskite film, revealing depth-dependent compositional heterogeneity. (d) Schematic illustration of the vapor-assisted hybrid two-step deposition process, highlighting the origin of incomplete conversion arising from limited diffusion of organic halide species through the compact inorganic framework.

to thicknesses of 50, 100, 200, and 400 nm, were systematically investigated (Figure 2b,c). A dilute $Al_2O_3$ NP dispersion was spin-coated onto the ITO/Me-4PACz substrate, resulting in sparse nanoparticle coverage of approximately 22%. Consistent with the proposed role of $Al_2O_3$ NPs, the surface energy of the substrate increased from 40.81 to 46.23 mN $m^{-1}$ upon NP incorporation, as evidenced by a reduced water contact angle (insets of Figure 2b,c; Figure S1). This increase in local surface energy is expected to lower the Gibbs free energy barrier for nucleation and reduce the critical nucleus radius on $Al_2O_3$ NPs relative to the surrounding Me-4PACz/ITO surface (Figure 2a). When the inorganic film was deposited on the control substrate, the initially smooth surface (root-mean-square roughness (rms) ≈ 3.2 nm) was preserved throughout growth, yielding a uniform and dense inorganic film with low roughness (≈ 4.24 nm; Figure 2b; Figures S2a and S3a). In contrast, films grown on substrates containing $Al_2O_3$ NPs exhibited a markedly different growth mode from the earliest stages (50 nm), with inorganic precursor crystals preferentially nucleating and growing on the sparsely distributed NP surfaces (Figure 2c). This localized heterogeneous nucleation behavior propagated throughout film growth, producing a relatively rough (rms ≈ 26.1 nm) and porous inorganic framework (Figure 2c; Figures S2b and S3b).

Beyond the pronounced topographical differences, such changes in growth mode are expected to directly influence the crystallographic orientation of the inorganic template. Grazing-incidence wide-angle X-ray scattering (GIWAXS) measurements were therefore employed to probe the orientation of the evaporated inorganic films. The incident angle was fixed at 2.0°, ensuring sufficient X-ray penetration through the entire inorganic layer while minimizing substrate scattering [27]. As shown in Figure 2d, the control film exhibits a sharp $PbI_2$ (001) reflection concentrated along the $q_z$ axis, indicative of a highly oriented layered structure with the c-axis perpendicular to the substrate. In contrast, films grown on substrates containing $Al_2O_3$ NPs display a noticeably broader azimuthal distribution of the $PbI_2$ (001) reflection, reflecting a diversification of crystallographic orientation. Quantitative analysis of the azimuthal intensity profiles reveals that the full width at half maximum (FWHM) of the $PbI_2$ (001) orientation

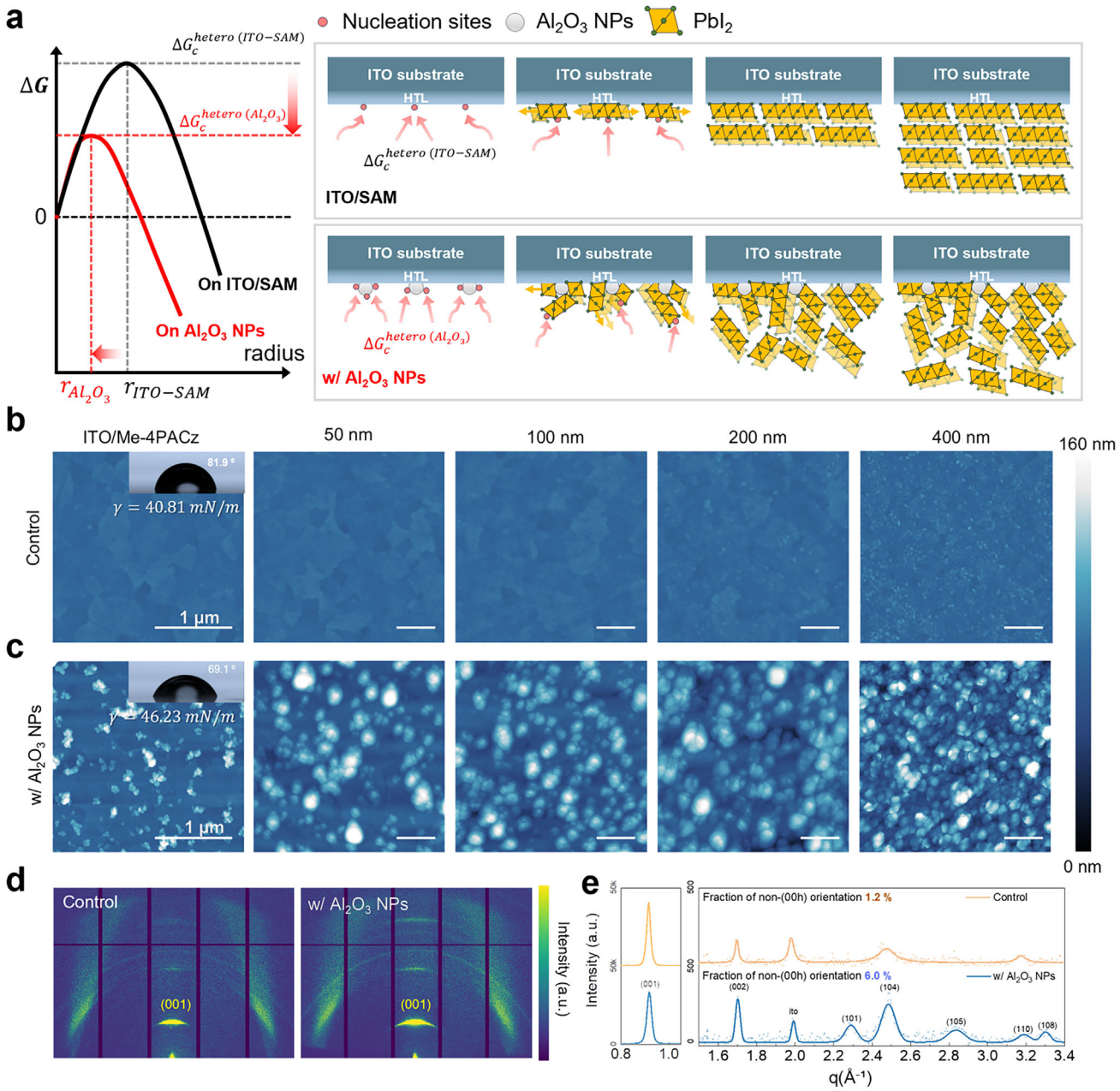


**FIGURE 2** | (a) Schematic illustration of the Gibbs free energy landscape for heterogeneous nucleation on ITO/SAM and $Al_2O_3$ nanoparticle (NP) surfaces, together with the corresponding growth behavior of inorganic films on bare ITO/SAM (control) and $Al_2O_3$ NP-modified substrates. Surface atomic force microscopy (AFM) images of thermally evaporated inorganic precursor layers with varying thicknesses (0, 50, 100, 200, and 400 nm) deposited on (b) control and (c) $Al_2O_3$ NP-modified substrates. Insets in the first panels show water contact angle measurements used to calculate the surface energies of the corresponding substrates. (d) Grazing-incidence wide-angle X-ray scattering (GIWAXS) patterns of inorganic films grown on control and $Al_2O_3$ NP-modified substrates. (e) Integrated GIWAXS peak intensity profiles as a function of scattering vector (q), obtained by integrating the azimuthal angle over −30° to 30°.

distribution increases from 13.0° in the control film to 17.35° in films deposited on $Al_2O_3$ NP-modified substrates, confirming a reduction in orientational order (Figure S4). Intensity line profiles as a function of scattering vector were extracted within a restricted azimuthal angle ($\chi$) window of −30° to 30° to preserve angular sensitivity while avoiding geometric distortions at higher $\chi$ values (Figure 2e). Peak indexing was performed after calibrating the q-axis using the GIWAXS pattern of a bare ITO substrate (Figure S5), whose characteristic diffraction features served as internal reference points. The diffraction profiles further reveal the emergence of additional $PbI_2$ reflections in films grown on $Al_2O_3$ NP-modified substrates, including the (101), (104), (105), and (110) planes. Quantitative analysis shows that the integrated intensity of these non-(00 h) $PbI_2$ reflections, normalized to the dominant (001) peak, increases from approximately 1.2% in the control film to 6.0% in the film incorporating $Al_2O_3$ NPs (Figure S6). This pronounced increase confirms that the introduction of localized heterogeneous nucleation sites effectively disrupts the

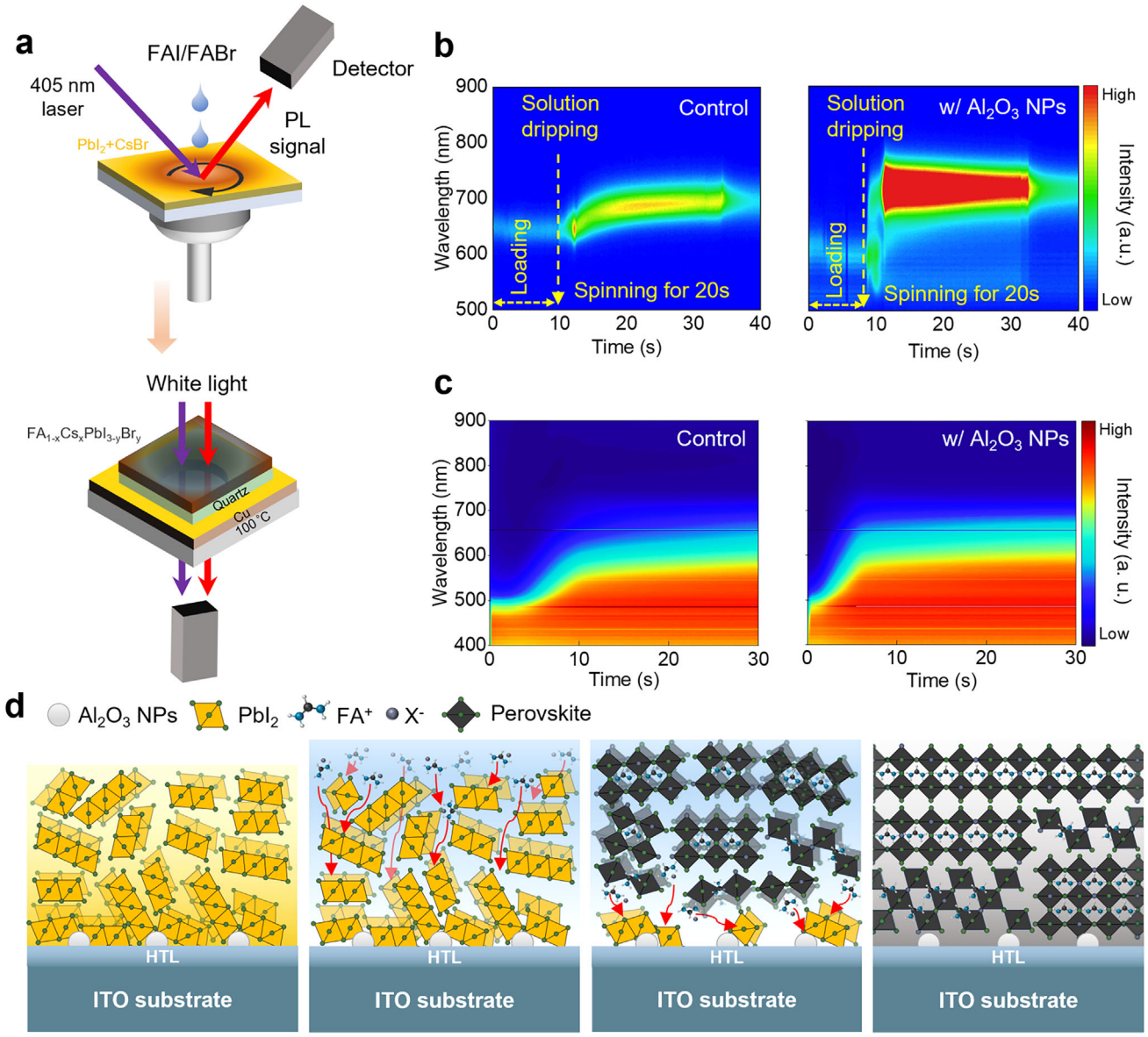


**FIGURE 3** | (a) Schematic illustration of the in situ steady-state photoluminescence (PL) and UV–vis absorption measurements performed during spin coating of the FAI/FABr solution onto the evaporated inorganic film, followed by thermal annealing. (b) In situ PL spectra of control and $Al_2O_3$ NP-modified films monitored during the spin-coating process of the FAI/FABr solution. (c) In situ UV–vis absorption spectra acquired from control and $Al_2O_3$ NP-modified films during the subsequent thermal annealing process. (d) Schematic illustration of the second-step reaction process facilitated by $Al_2O_3$ NP-induced heterogeneous nucleation.

strong (001) texture, thereby modifying both the morphology and crystallographic orientation of the inorganic framework.

To elucidate how this modified inorganic template influences the subsequent conversion kinetics, in situ photoluminescence (PL) and UV–vis absorption measurements were performed during the spinning and annealing steps, respectively (Figure 3a). These techniques enable real-time monitoring of the optical evolution associated with the transformation of the inorganic precursor into the perovskite phase, providing kinetic insight complementary to the structural analyses discussed above. For the control sample, the in situ PL spectra initially exhibit an emission peak centered at approximately 650 nm, which gradually red-shifts toward ~700 nm as the reaction proceeds (Figure 3b; Figure S7). This gradual red shift is commonly attributed to the evolution of quantum-confined perovskite nuclei and/or progressive compositional homogenization during the diffusion and reaction of FAI/FABr with the underlying inorganic layer [28, 29]. In contrast, films formed on $Al_2O_3$ NP-modified substrates display a markedly different PL evolution. From the onset of detectable emission, the PL peak is centered at ~728 nm and remains essentially unchanged throughout the monitored period, while the overall PL intensity is significantly higher than that of the control sample. The absence of an initial blue-shifted emission, together with the enhanced PL intensity, suggests that diffusion and reaction of FAI/FABr occur more rapidly and uniformly, leading to the simultaneous formation of a higher density of optically active perovskite nuclei.

The evolution of UV–vis absorption spectra during the annealing step further highlights the accelerated conversion kinetics induced by $Al_2O_3$ NPs (Figure 3c). During annealing, FAI and FABr precursors continue to diffuse into the inorganic layer and promote rearrangement of the inorganic framework into corner-sharing $PbX_6$ octahedra. This process is reflected by a progressive red shift of the absorption edge and an overall increase in absorbance at early annealing stages. In the presence of $Al_2O_3$ NPs, the absorbance near the perovskite band edge increases rapidly and reaches a stable spectral profile within a significantly shorter time window (Figures S8 and S9). By contrast, the control film exhibits a much slower absorbance build-up, with the band edge requiring considerably longer annealing time to reach its steady-state position. The extended rise time of absorption in the long-wavelength region indicates delayed formation of optically active perovskite domains in the control film. Collectively, the accelerated PL emergence and faster absorption evolution observed for films incorporating $Al_2O_3$ NPs provide strong evidence that the modified inorganic framework facilitates diffusion and reaction of FAI/FABr, thereby alleviating reaction-limited phase formation during the hybrid two-step deposition process.

The morphology, crystallographic structure, and optoelectronic properties of the perovskite films are investigated in Figure 4a–d. Both the control film and the film incorporating $Al_2O_3$ NPs exhibit a similar optical bandgap of approximately 1.7 eV (Figure S10), indicating that the introduction of $Al_2O_3$ NPs does not alter the perovskite composition. Because halide incorporation in the present hybrid two-step process proceeds via solution-mediated conversion, the measured bandgap is interpreted using composition–bandgap relationships established for solution-processed mixed-halide perovskites. Within this framework, the observed bandgap of ~1.7 eV at Cs ≈ 16% corresponds to a mixed-halide regime with an estimated Br fraction on the order of ~25%–30% [30, 31]. Notably, the film grown with $Al_2O_3$ NPs shows slightly enhanced optical absorption compared with the control film. Atomic force microscopy (AFM) images (Figure 4a,b) reveal that perovskite films formed on $Al_2O_3$ NP-modified substrates possess a larger average grain size of 0.85 ± 0.22 μm, compared with 0.67 ± 0.16 μm for films deposited on ITO/Me-4PACz substrates (Figure S11). XRD analysis further indicates a substantial reduction in residual $PbI_2$ content, decreasing from approximately 30% in the control film to 8% in the film incorporating $Al_2O_3$ NPs (Figure 4c). Consistent with this observation, ToF-SIMS depth profiling reveals a more uniform vertical distribution of $FA^+$ species and a suppressed $Pb^+$ accumulation near the buried interface in films incorporating $Al_2O_3$ NPs (Figure S12), indicating enhanced $FA^+$ diffusivity during the solution-mediated conversion process. This improved mass transport facilitates more complete reaction throughout the film thickness, effectively reducing residual $PbI_2$ at the bottom interface. In addition, the relative intensity of the (111) diffraction peak is enhanced in the $Al_2O_3$ NP-assisted film, indicating an increased fraction of (111)-oriented crystal facets along the out-of-plane direction (Figure S13). The enhanced formation of higher-surface-energy (111) facets, compared to the low-energy (001) facets, is likely associated with the diversified orientation of the underlying inorganic framework induced by localized heterogeneous nucleation [32]. Steady-state and time-resolved photoluminescence (PL) measurements (Figure 4d) provide direct evidence of improved optoelectronic quality. The $Al_2O_3$ NP-assisted film exhibits both enhanced PL intensity and a prolonged carrier lifetime (89.34 ns), compared with the control film (65.41 ns; Table S1). These improvements are attributed to more complete precursor conversion, reduced residual $PbI_2$, and promoted grain growth, which collectively suppress non-radiative recombination pathways.

The photovoltaic performance of wide-bandgap PSCs fabricated using control films and films incorporating different concentrations of $Al_2O_3$ NPs is presented in Figure 4e–g, with average device parameters summarized in Table S2. The control device delivers a power conversion efficiency (PCE) of 18.62% (stabilized 17.92%; Figure 4f), with a short-circuit current density ($J_{SC}$) of 20.31 mA $cm^{-2}$, an open-circuit voltage ($V_{OC}$) of 1.190 V, and a fill factor (*FF*) of 0.77. As the $Al_2O_3$ NP solution concentration increases from 0.05 to 0.15 wt.%, both $J_{SC}$ and *FF* gradually improve, while $V_{OC}$ exhibits a slight decrease. The *PCE* of 20.20% (stabilized 19.65%) is achieved at an optimal $Al_2O_3$ NP concentration of 0.15 wt.%, with a $J_{SC}$ of 21.17 mA $cm^{-2}$, a $V_{OC}$ of 1.185 V, and an *FF* of 0.81. The enhancement in $J_{SC}$ primarily originates from an increase in external quantum efficiency (*EQE*) in the short-wavelength region (Figure 4g), which is likely associated with improved charge carrier generation and collection near the bottom interface. This improvement is consistent with the reduced residual $PbI_2$ at the buried interface enabled by more complete reaction in films grown with $Al_2O_3$ NPs [33]. Further increasing the $Al_2O_3$ NP concentration to 0.2 wt.% leads to degraded device performance (Figure S14), likely due to excessive nanoparticle coverage (~66%; Figure S15). With the optimized $Al_2O_3$ NP concentration, additional surface passivation of the perovskite film yields a champion device *PCE* of 21.23% (stabilized 20.93%), with a $J_{SC}$ of 20.92 mA $cm^{-2}$ (integrated $J_{SC}$ from *EQE* ≈ 20.53 mA $cm^{-2}$; Figure S16), a $V_{OC}$ of 1.223 V, and an FF of 0.83.

Owing to the more complete reaction between FAI/FABr and $PbI_2$, perovskite films incorporating $Al_2O_3$ NPs are expected to contain fewer residual precursors than control films, particularly excess FAI/FABr near the top surface and unreacted $PbI_2$ at the bottom interface. Such residual precursors are known to introduce defect states and promote parasitic processes, including ion migration and interfacial side reactions. Moreover, off-stoichiometric regions at the top and bottom surfaces can induce unintended self-doping effects, leading to unfavorable energetic band bending within the perovskite layer (Figure S18). Consistent with this expectation, the surface of the control perovskite film exhibits a higher work function, corresponding to more pronounced p-type character, than that of the film incorporating $Al_2O_3$ NPs (Figure 5a). This behavior is attributed to excess FAI/FABr at the top surface of the control film. Conversely, the $PbI_2$-rich region near the bottom interface of the control film is observed to exhibit a lower work function, indicative of n-type character. The resulting inverted n/p internal junction within an overall p-i-n device architecture is detrimental to efficient charge extraction. In addition, residual insulating $PbI_2$ at the buried interface acts as an additional barrier for photogenerated hole extraction, further compromising device performance.

In Figure 5b, the operational stability of the control and $Al_2O_3$ NP devices was evaluated at 60°C under 1-sun illumination

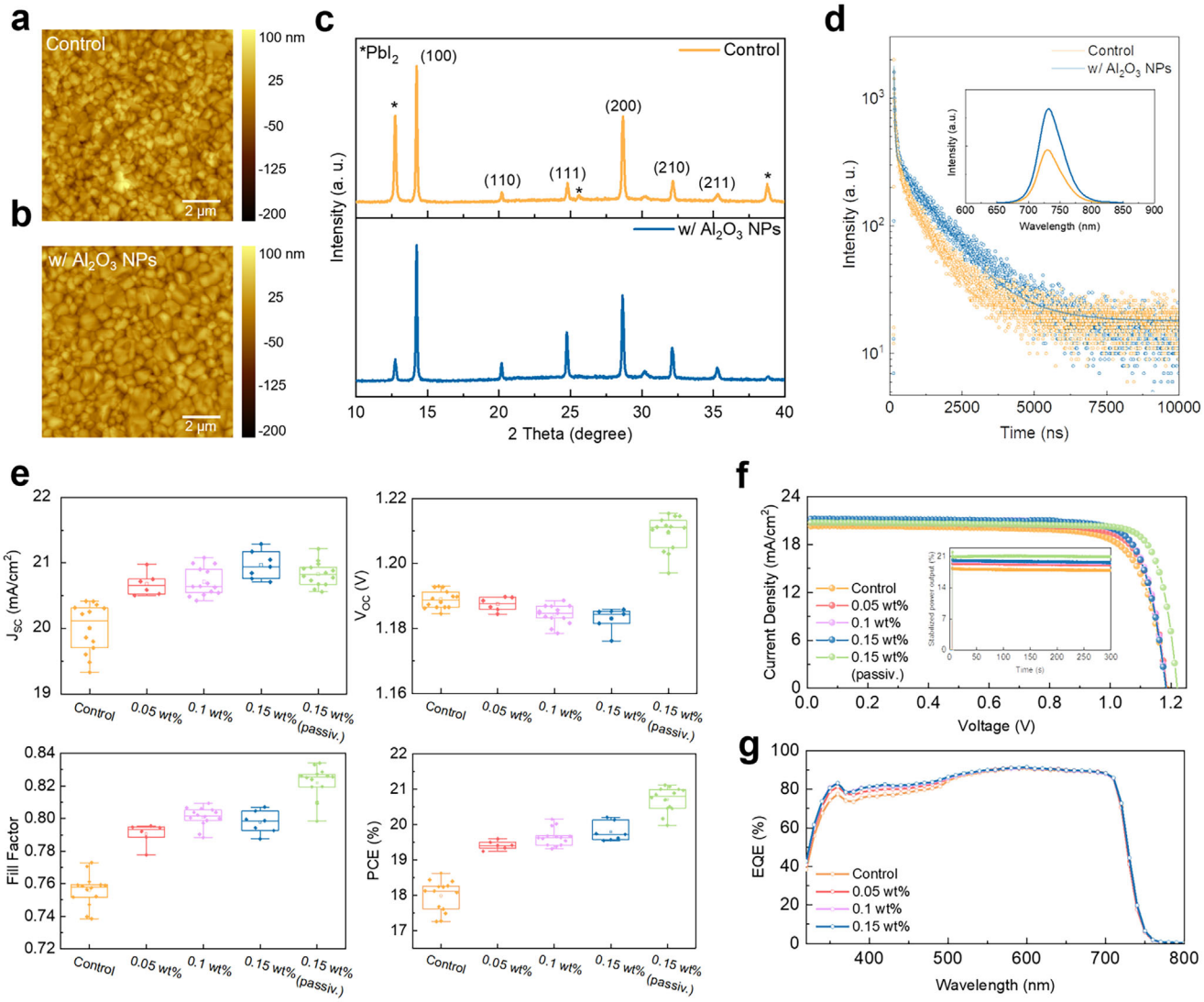


**FIGURE 4** | Surface atomic force microscopy (AFM) images of perovskite films deposited on (a) control and (b) $Al_2O_3$ NP-modified substrates. (c) X-ray diffraction (XRD) patterns of the corresponding perovskite films. (d) Time-resolved photoluminescence (TRPL) spectra of control and $Al_2O_3$ NP-modified perovskite films, with the inset showing the corresponding steady-state PL spectra. (e) Statistical distributions of short-circuit current density ($J_{SC}$), open-circuit voltage ($V_{OC}$), fill factor (FF), and power conversion efficiency (PCE) for devices fabricated with varying $Al_2O_3$ NP solution concentrations (0, 0.05, 0.10, and 0.15 wt.%), together with devices incorporating top-surface passivation at the optimal concentration (0.15 wt.%_passiv.). (f) Corresponding current density–voltage (*J–V*) curves, with the inset showing the stabilized power output (SPO) of the best-performing devices under each condition. (g) External quantum efficiency (EQE) spectra of the corresponding devices with varying $Al_2O_3$ NP solution concentrations.

and constant bias voltage. The control device exhibits rapid degradation, reaching $T_{80}$ (defined as the time required for the *PCE* to decay to 80% of its initial value) within 100 h. In contrast, devices incorporating 0.15 wt.% $Al_2O_3$ NPs demonstrate a significantly prolonged operational lifetime, with $T_{80}$ exceeding 200 h. Thermal stability was further assessed by aging devices at 75°C in a nitrogen-filled glovebox (Figure 5c). While control devices retain approximately 90% of their initial efficiency after ~ 400 h of thermal stress, devices fabricated with 0.15 wt.% $Al_2O_3$ NPs preserve more than 97% of their initial efficiency even after 900 h. The substantially extended device lifetime highlights the critical role of $Al_2O_3$ NP-assisted heterogeneous nucleation in promoting more complete precursor conversion, suppressing interfacial defects, and improving internal energetics [34, 35]. Collectively, these effects enable simultaneous enhancement of performance and operational durability in wide-bandgap PSCs fabricated via hybrid two-step deposition processes.

In addition, to assess potential UV-induced degradation effects, complementary stability measurements were performed under UV-containing xenon lamp illumination, with the corresponding stabilized power output data and light-source emission spectra provided in the Supporting Information (Figure S19). Under the UV-inclusive conditions (~40°C, ~25% RH, without encapsulation), devices incorporating $Al_2O_3$ nanoparticles consistently exhibited improved stability compared to the control devices, confirming that the observed stability enhancement is maintained under UV-relevant stress conditions.

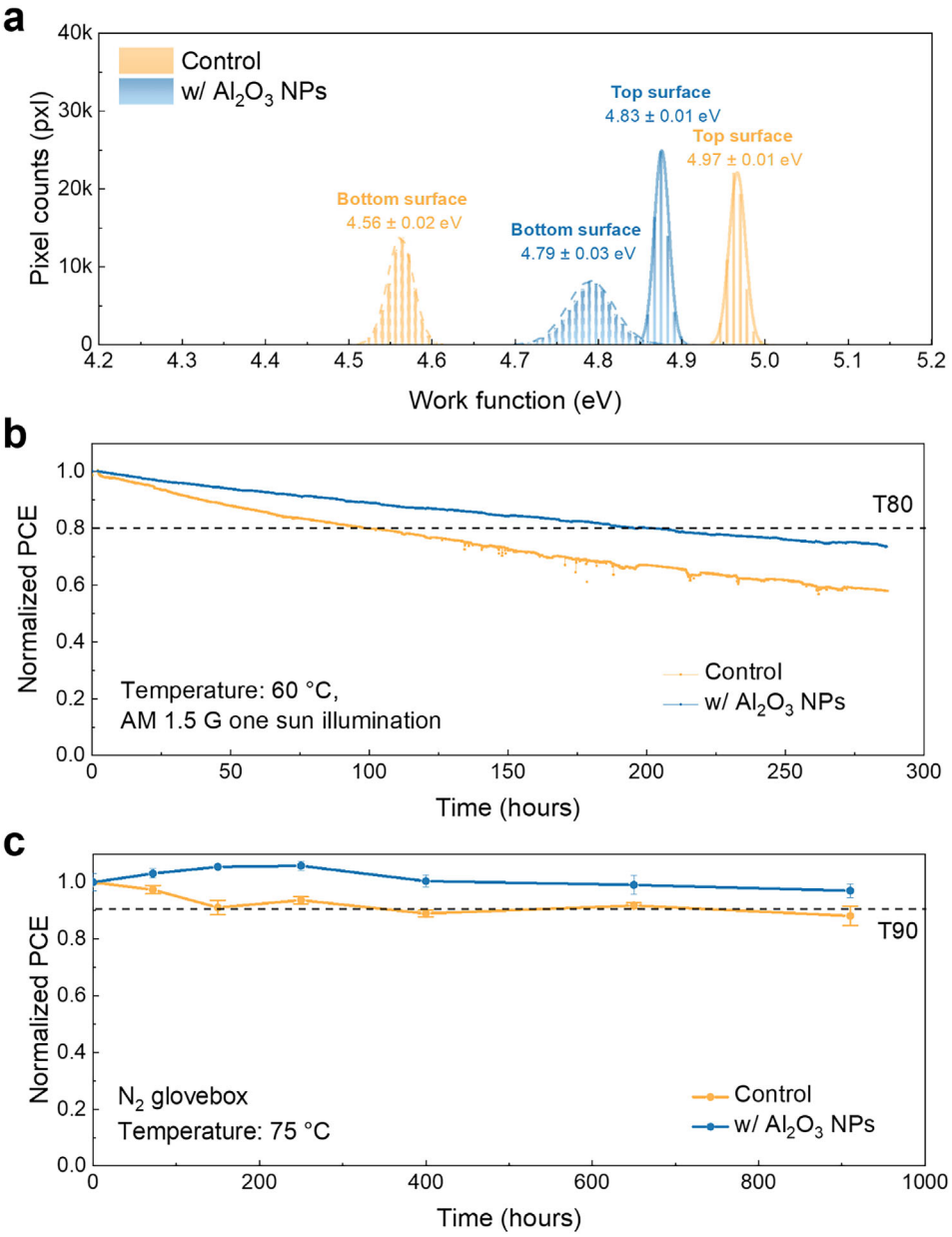


**FIGURE 5** | (a) Kelvin probe force microscopy (KPFM)–derived work-function distributions of the top and bottom surfaces of the control and w/ $Al_2O_3$ NPs–containing perovskite films, presented as histograms extracted from the corresponding surface potential maps. (b) Operational stability of encapsulated control and 0.15 wt.% $Al_2O_3$ NP-based devices measured at 60°C under continuous 1-sun AM 1.5G simulated illumination (LED source) and constant bias voltage. (c) Thermal stability of the corresponding devices was evaluated under dark conditions at 75°C. Each data point represents the average power conversion efficiency (PCE), with error bars indicating the standard deviation obtained from more than five devices measured under each condition.

## 3 | Conclusion

In conclusion, we have identified that reaction-limited phase formation in vapor-assisted hybrid two-step deposition of halide perovskites primarily originates from the compact, non-porous, and highly crystalline inorganic layers formed by thermal evaporation. Such dense inorganic frameworks severely restrict the incorporation of organic halides, leading to incomplete conversion and pronounced depth-dependent heterogeneity. To overcome this limitation, we introduced localized heterogeneous nucleation sites with higher surface energy to deliberately regulate nucleation and early-stage growth of the inorganic layer. Sparsely dispersed hydrophilic metal oxide species act as effective heterogeneous nucleation centers during vapor deposition, yielding a rougher, more porous inorganic framework with a relaxed layered structure. This engineered inorganic template substantially facilitates organic halide diffusion and incorporation during the subsequent solution-assisted step, thereby alleviating reaction limitations and suppressing residual unreacted precursors. As a result, the perovskite films exhibit improved stoichiometric uniformity, enhanced optoelectronic quality, and reduced vertical heterogeneity. Importantly, these material-level

improvements directly translate into wide-bandgap perovskite solar cells with significantly enhanced power conversion efficiency and operational stability. Beyond the specific system studied here, we believe that this work provides a general framework for crystal growth engineering of vapor-deposited perovskite thin films.


### Acknowledgements

This study was supported by a National Research Foundation of Korea (NRF) grant funded by the Korean government (Ministry of Science and ICT) under contract numbers RS-2024-00416154 and RS-2025-00522377. T.K. acknowledges support from the U.S. Department of Energy (DOE), Office of Science, Office of Basic Energy Sciences, Materials Sciences and Engineering Division under contract no. DE-AC02-05-CH11231 (D2S2 program KCD2S2). Work at the Molecular Foundry was supported by the Office of Science, Office of Basic Energy Sciences of the U.S. Department of Energy under Contract No. DE-AC02-05CH11231. Work at the Advanced Light Source (ALS) was done at beamline 12.3.2. The ALS is a DOE Office of Science User Facility under Contract No. DE-AC02-05CH11231. The authors acknowledge the use of OpenAI's ChatGPT-4o for language editing support.


### Conflicts of Interest

The authors declare no conflicts of interest.

### Data Availability Statement

All data needed to evaluate the conclusions in the paper are present in the paper or the supplementary materials.

### References


1. Z. Xiong, Q. Zhang, K. Cai, et al., "Homogenized Chlorine Distribution for >27% Power Conversion Efficiency in Perovskite Solar Cells," *Science* 390 (2025): 638–642, https://doi.org/10.1126/science.adw8780.

2. S. Tan, M.-C. Shih, Y. Lu, et al., "Spontaneous Formation of Robust Two-Dimensional Perovskite Phases," *Science* 388 (2025): 639–645, https://doi.org/10.1126/science.adr1334.

3. National Renewable Energy Laboratory 2025 (2025).

4. J. H. Lee, B. S. Kim, J. Park, J. W. Lee, and K. Kim, "Opportunities and Challenges for Perovskite Solar Cells Based on Vacuum Thermal Evaporation," *Advanced Materials Technologies* 8 (2023): 2200928, https://doi.org/10.1002/admt.202200928.

5. J. Avila, C. Momblona, P. P. Boix, M. Sessolo, and H. J. Bolink, "Vapor-Deposited Perovskites: the Route to High-Performance Solar Cell Production?," *Joule* 1 (2017): 431–442, https://doi.org/10.1016/j.joule.2017.07.014.

6. X. Y. Chin, D. Turkay, J. A. Steele, et al., "Interface Passivation for 31.25%-Efficient Perovskite/Silicon Tandem Solar Cells," *Science* 381 (2023): 59–63, https://doi.org/10.1126/science.adg0091.

7. O. Er-raji, C. Messmer, R. R. Pradhan, et al., "Electron Accumulation across the Perovskite Layer Enhances Tandem Solar Cells with Textured Silicon," *Science* 390 (2025): adx1745, https://doi.org/10.1126/science.adx1745.

8. X. Zheng, W. Kong, J. Wen, et al., "Solvent Engineering for Scalable Fabrication of Perovskite/Silicon Tandem Solar Cells in Air," *Nature Communications* 15 (2024): 4907, https://doi.org/10.1038/s41467-024-49351-5.

9. E. Aydin, T. G. Allen, and M. De Bastiani, "Pathways toward Commercial Perovskite/Silicon Tandem Photovoltaics," *Science* 383 (2024): adh3849, https://doi.org/10.1126/science.adh3849.

10. H.-S. Ko, J.-W. Lee, and N.-G. Park, "15.76% efficiency Perovskite Solar Cells Prepared under High Relative Humidity: Importance of $PbI_2$ Morphology in Two-Step Deposition of $CH_3NH_3PbI_3$," *Journal of Materials Chemistry A* 3 (2015): 8808–8815, https://doi.org/10.1039/C5TA00658A.

11. F. Wang, T. Wang, Y. Sun, et al., "Two-Step Perovskite Solar Cells with>25% Efficiency: Unveiling the Hidden Bottom Surface of Perovskite Layer," *Advanced Materials* 36 (2024): 2401476.

12. W. S. Yang, J. H. Noh, N. J. Jeon, et al., "High-Performance Photovoltaic Perovskite Layers Fabricated through Intramolecular Exchange," *Science* 348 (2015): 1234–1237, https://doi.org/10.1126/science.aaa9272.

13. H. Luo, X. Zheng, W. Kong, et al., "Inorganic Framework Composition Engineering for Scalable Fabrication of Perovskite/Silicon Tandem Solar Cells," *ACS Energy Letters* 8 (2023): 4993–5002, https://doi.org/10.1021/acsenergylett.3c02002.

14. J. Fang, W. Chen, S. Yuan, et al., "Longitudinal Homogenized Intermediates Facilitate Air-Processed Hybrid Sequential Deposition of Perovskite/Silicon Tandem Solar Cells," *ACS Materials Letters* 6 (2024): 5066–5075, https://doi.org/10.1021/acsmaterialslett.4c01687.

15. Z. Li, J. Li, H. Cao, et al., "Surface-Orientation Elimination of Vapor-Deposited $PbI_2$ Flakes for Efficient Perovskite Synthesis on Curved Solar Cells," *ACS Applied Materials & Interfaces* 13 (2021): 45496–45504, https://doi.org/10.1021/acsami.1c12283.

16. F. Wang, P. Wai-Keung Fong, Z. Ren, et al., "In-Depth Understanding of Ionic Liquid Assisted Perovskite Film Formation Mechanism for Two-Step Perovskite Photovoltaics," *Journal of Energy Chemistry* 73 (2022): 599–606, https://doi.org/10.1016/j.jechem.2022.06.040.

17. A. Ummadisingu and M. Grätzel, "Revealing the Detailed Path of Sequential Deposition for Metal Halide Perovskite Formation," *Science advances* 4 (2018): 1701402, https://doi.org/10.1126/sciadv.1701402.

18. B. P. Dhamaniya, P. Chhillar, A. Kumar, et al., "Orientation-Controlled (h0l) $PbI_2$ Crystallites Using a Novel Pb–Precursor for Facile and Quick Sequential $MAPbI_3$ Perovskite Deposition," *ACS Omega* 5 (2020): 31180–31191, https://doi.org/10.1021/acsomega.0c04483.

19. D. Huang, Q. Liu, Z. Ma, et al., "Orientation-Controlled Mesoporous $PbI_2$ Scaffold for 22.7% Perovskite Solar Cells," *Science China Materials* 66 (2023): 1313–1322, https://doi.org/10.1007/s40843-022-2289-5.

20. P. Cui, D. Wei, J. Ji, et al., "Planar p–n Homojunction Perovskite Solar Cells with Efficiency Exceeding 21.3%.3%," *Nature Energy* 4 (2019): 150–159, https://doi.org/10.1038/s41560-018-0324-8.

21. W.-J. Yin, T. Shi, and Y. Yan, "Unusual Defect Physics in $CH_3NH_3PbI_3$ Perovskite Solar Cell Absorber," *Applied Physics Letters* 104 (2014): 063903, https://doi.org/10.1063/1.4864778.

22. S. Tan, I. Yavuz, M. H. Weber, et al., "Shallow Iodine Defects Accelerate the Degradation of $\alpha$-Phase Formamidinium Perovskite," *Joule* 4 (2020): 2426–2442, https://doi.org/10.1016/j.joule.2020.08.016.

23. C. Dong, D. Liu, L. Wang, et al., "Growth Mechanism of Thermally Evaporated $\gamma$-$CsPbI_3$ Film," *Advanced Functional Materials* 33 (2023): 2214414, https://doi.org/10.1002/adfm.202214414.

24. C. Ran, W. Gao, N. Li, et al., "Facet-Dependent Control of $PbI_2$ Colloids for over 20% Efficient Perovskite Solar Cells," *ACS Energy Letters* 4 (2018): 358–367, https://doi.org/10.1021/acsenergylett.8b02262.

25. W. Peng, K. Mao, F. Cai, et al., "Reducing Nonradiative Recombination in Perovskite Solar Cells with a Porous Insulator Contact," *Science* 379 (2023): 683–690, https://doi.org/10.1126/science.ade3126.

26. J.-W. Lee and S. M. Kang, "Patterning of Metal Halide Perovskite Thin Films and Functional Layers for Optoelectronic Applications," *Nano-Micro Letters* 15 (2023): 184, https://doi.org/10.1007/s40820-023-01154-x.

27. D.-K. Lee, K. Fykouras, T. Kodalle, et al., "Strain Engineering: Reduction of Microstrain at the Perovskite Surface via Alkali Metal Chloride Treatment Enhances Stability," *ACS Energy Letters* 10 (2025): 1039–1049, https://doi.org/10.1021/acsenergylett.4c03334.

28. K. Park, D. Zhang, and D.-K. Lee, "Elucidating Compositional Differences in Halide Perovskites for Normal and Inverted Perovskite Solar Cells," *ACS Energy Letters* 11 (2025): 548–556.

29. T. Huang, S. Tan, S. Nuryyeva, et al., "Performance-Limiting Formation Dynamics in Mixed-Halide Perovskites," *Science advances* 7 (2021): abj1799, https://doi.org/10.1126/sciadv.abj1799.

30. K. A. Bush, K. Frohna, R. Prasanna, et al., "Compositional Engineering for Efficient Wide Band Gap Perovskites with Improved Stability to Photoinduced Phase Segregation," *ACS Energy Letters* 3 (2018): 428–435, https://doi.org/10.1021/acsenergylett.7b01255.

31. L. Gil-Escrig, C. Dreessen, F. Palazon, et al., "Efficient Wide-Bandgap Mixed-Cation and Mixed-Halide Perovskite Solar Cells by Vacuum Deposition," *ACS Energy Letters* 6 (2021): 827–836, https://doi.org/10.1021/acsenergylett.0c02445.

32. J.-W. Lee, S. Tan, T.-H. Han, et al., "Solid-Phase Hetero Epitaxial Growth of $\alpha$-Phase Formamidinium Perovskite," *Nature Communications* 11 (2020): 5514, https://doi.org/10.1038/s41467-020-19237-3.

33. H. Shim, S. Seo, C. Chandler, et al., "Enhancing Radiation Resilience of Wide-Band-Gap Perovskite Solar Cells for Space Applications via a-Site Cation Stabilization with $PDAI_2$," *Joule* 9 (2025): 102043, https://doi.org/10.1016/j.joule.2025.102043.

34. S. R. Lee, D. Lee, S. G. Choi, et al., "Accelerated Degradation of $FAPbI_3$ Perovskite by Excess Charge Carriers and Humidity," *Solar RRL* 8 (2024): 2300958, https://doi.org/10.1002/solr.202300958.

35. S. Tan, T. Huang, I. Yavuz, et al., "Stability-Limiting Heterointerfaces of Perovskite Photovoltaics," *Nature* 605 (2022): 268–273, https://doi.org/10.1038/s41586-022-04604-5.

## Supporting Information

Additional supporting information can be found online in the Supporting Information section.

**Supporting File**: aenm70838-sup-0001-SuppMat.docx.